# Fabrication of Y-Splitters and Mach-Zehnder Structures on (Yb,Nb):$RbTiOPO_4$/$RbTiOPO_4$ Epitaxial Layers by Reactive Ion Etching

M. A. Butt, R. Solé, M. C. Pujol, A. Ródenas, G. Lifante, A. Choudhary, G. S. Murugan, D. P. Shepherd, J. S. Wilkinson, M. Aguiló, and F. Díaz

***Abstract*—Reactive ion etching of $RbTiOPO_4$ (001) substrates and (Yb,Nb):$RbTiOPO_4$/$RbTiOPO_4$ (001) epitaxial layers has been performed using fluorine chemistry. A maximum etch rate of 8.7 nm/min was obtained, and the deepest etch achieved was 3.5 μm. The (Yb,Nb)-doped epitaxial layers showed a slower etching rate when compared with undoped material. Liquid phase epitaxial growth of cladding layers has also been performed, resulting in a high-quality interface growth without appreciable defects. 9-mm-long Mach Zehnder interferometer (MZI) and 9-mm-long Y-splitter structures were designed and patterned in $RbTiOPO_4$ substrates and (Yb,Nb):$RbTiOPO_4$/$RbTiOPO_4$ (001) epitaxial layers. The structures fabricated in $RbTiOPO_4$ substrates were filled with laser active (Yb,Nb):$RbTiOPO_4$ higher refractive index core material, and finally an $RbTiOPO_4$ cladding was grown on the samples. The refractive index difference between the (Yb,Nb):$RbTiOPO_4$ layer and the $RbTiOPO_4$ substrate at 1.5 μm has been measured and optical waveguiding at this wavelength has been demonstrated.**

***Index Terms*—Integrated Optical Materials, $RbTiOPO_4$, Reactive Ion Etching, optical waves.**

## I. Introduction

$RbTiOPO_4$ (hereafter RTP) belongs to the $KTiOPO_4$ (KTP) family of nonlinear optical crystals. These crystals are orthorhombic and positive biaxial, with a=12.974(2) Å, b=6.494(3) Å and c=10.564(6) Å [1] with the space group $Pna2_1$ and $n_x<n_y<n_z$ (being the X, Y, and Z, the dielectric axes parallel to the crystallographic ***a***, ***b***, and ***c*** directions, respectively). RTP has large electro-optical coefficients (i.e. $r_{33}$=39.3 pm/V) and, high nonlinear optical coefficients (i.e. $d_{33}$= 15.6±0.3 pm/V) [2], which make them attractive for electro-optic applications such as modulators and Q-switches [3]. These electro-optic properties also make RTP an attractive material for integrated optical applications for fabrication of active and passive devices. Traditionally, in the KTP family of crystals, such devices are fabricated by ion diffusion techniques; in which a graded refractive index profile is achieved [4] leading to channel waveguides if the diffusion is carried out through an appropriate mask. Ion implantation has been also used as a feasible technique to obtain waveguides with graded refractive index profile in RTP recently [5,6]. Planar optical waveguides have already been demonstrated, for guiding light in the near infrared (NIR) and visible range, based on (Yb,Nb):RTP/RTP (001) epitaxial layers and, in contrast to diffused and ion implanted waveguides, these systems possess a step-index profile [7].

Reactive ion etching (RIE), as commonly is used for structuring dielectric materials such as $SiO_2$ and $LiNbO_3$ [8-11], could be used to produce channel waveguides in (Yb,Nb):RTP/RTP (001) planar layers and RTP (001) substrates. However, the use of this technique in the KTP family of compounds has not yet been widely explored. Dubs *et al.* reported the preparation of ridge type waveguide structures on $K_{1-x}Rb_xTiOPO_4$/KTP epitaxial layers by electron-cyclotron-resonance reactive ion etching (ECR-RIE) obtaining results in a 3.5 μm depth etch channel [12].

Initially, it would be desirable to use undoped KTP or RTP hosts as active waveguide layer materials if only the electro-optic properties should be used. In this case the substrate material with lower refractive index than the core would be an isostructural material with a ionic substitution in the $K^+$ or $Rb^+$ position (Ti or P elements cannot be substituted for any lighter element in order to decrease the refractive index and maintain the crystalline structure) and if in the substrate or in the active epitaxial layer, part of the $K^+$ or $Rb^+$ cations are substituted by other monovalent cations for obtaining differences in the refractive index between the substrate and the layer, the refractive index profile along ***c*** direction is graded, because of the high ionic conductivity in this direction in KTP and RTP compounds [13]. This fact induces that the active layer should be the doped one; and the substitution should be preferably in the Ti position; then using the couple (Yb,Nb) already used in the past for RTP, is logical due to the charge compensation in the compound (doping only with $Nb^{5+}$ can create more $Rb^+$

This work was supported by the Spanish Government under the Project MAT2013-47395-C4-4-R, by the Catalan Authority under Project 2014SGR1358. M. Ali Butt thanks the Catalan Government for the FI-DGR fellowship 2012FI-B 00192. A. Choudhary acknowledges an UK Engineering and Physical Sciences Research Council (EPSRC) doctoral prize.

M. A. Butt, , R. Solé, M. C. Pujol, A. Ródenas, M. Aguiló and F. Díaz are with Física i Cristal·lografia de Materials i Nanomaterials (FiCMA-FiCNA) and EMaS, Universitat Rovira i Virgili (URV), Marcel·lí Domingo s/n, E-43007 Tarragona, Spain (email authors: muhammadali.butt@urv.cat, rosam.sole@urv.cat, mariacinta.pujol@urv.cat, airan.rodenas@urv.cat, magdalena.aguiló@urv.cat and f.diaz@urv.cat).

G. Lifante is with the Departamento de Física de Materiales, Universidad Autónoma de Madrid E-28049 Madrid, Spain (email author: gines.lifante@uam.es).

A. Choudhary, G. S. Murugan, D. P. Shepherd and J. S. Wilkinson are with the Optoelectronics Research Centre, University of Southampton, Southampton, SO171BJ, United Kingdom (email authors: ac12g10@orc.soton.ac.uk, smg@orc.soton.ac.uk, dps@orc.soton.ac.uk, jsw@ecs.soton.ac.uk).

vacancies [14]) and the future possibility to use $Yb^{3+}$ ion as active ion for laser and SFD emission. Then, the chemical composition of the epitaxies used in this work is (Yb,Nb):RTP layers over undoped RTP, despite the future applications of the designed devices in the present work is only based in the electro-optic properties of these compounds.

Our previous work showed the first exploratory research of the optima conditions for RIE etching in (Yb,Nb):RTP epitaxial layers to obtain channel waveguides with a height around 1.5 μm [15]. In this work, waveguides with larger dimensions than the previous ones reported were designed in order to confine 1.5 μm wavelength radiations; this wavelength is especially interesting in the telecommunications and biomedical fields. The etching has been performed both in the active layer and in the undoped substrate, and consequently, in order to obtain the guiding composite, one or two epitaxial growth processes were required. Finally, the fabricated waveguide structures were optically characterized.

## II. WAVEGUIDE FABRICATION

### *A. Substrate growth by TSSG and epitaxial growth by LPE*

RTP melts incongruently, and it cannot be grown directly from the melt, then high temperature solution growth and hydrothermal methods have been used traditionally to grow these crystals [16]. In this work, the top-seeded solution growth-slow cooling (TSSG-SC) technique was applied to grow RTP single crystals to be used for substrates [17]. All growth experiments were performed in a vertical tubular single-zone furnace. The solution composition was chosen taking into account the RTP primary crystallization region in solutions with 20 mol% $WO_3$ [18]. The solution composition used was $Rb_2O$-$P_2O_5$-$TiO_2$-$WO_3$=44.24-18.96-16.8-20 (mol %). Solutions weighing around 200 g were prepared by mixing $Rb_2CO_3$ (99%), $NH_4H_2PO_4$ (99%), $TiO_2$ (99%) and $WO_3$ (99%). The solution was homogenized at a temperature around 50 K above the expected saturation temperature for a few hours. The saturation temperature was determined with a ***c***-oriented RTP seed crystal in contact with the center of the solution surface and rotating at 60 rpm. For this solution, the saturation temperature was around 1163 K. After that, the supersaturation of the solution was obtained by applying slow cooling to the solution at a rate of 0.1 K/h for the first 15 K and then 0.05 K/h for the next 10-20 K. The crystal rotation was 60 rpm in the initial steps of growth and as the crystal was growing, the rotation was decreased progressively to 40 rpm in order to maintain the convection pattern. In several experiments, when the crystal dimension in the (001) plane was enough, a pulling rate of 1 mm per day was applied in order to increase the crystal dimension along the ***c*** direction. When the crystal was fully grown, it was slowly extracted from the solution and maintained slightly above the solution surface whereas the furnace was cooled at 30-40 K/h to room temperature. Finally, the substrates for LPE growth were obtained by cutting, with a diamond saw, the bulk crystals in slices perpendicular to the crystallographic ***c*** direction. After cutting, the substrates were polished with diamond powder.

The liquid phase epitaxy (LPE) technique was used to obtain (Yb,Nb):RTP/RTP(001) epitaxial layers [19]. The experiments were carried out in a well-isolated vertical cylindrical furnace, with a central region with practically no thermal gradients.

The solution composition used in these LPE experiments was $Rb_2O$-$P_2O_5$-$TiO_2$-$Nb_2O_5$-$Yb_2O_3$-$WO_3$=43.9-23.6-20.7-0.45-1.35-10 (mol %). The reagents used were the same as in the growth of substrates and $Yb_2O_3$ (99.9 %) and $Nb_2O_5$ (99.9 %) were used for doping. Cylindrical crucibles of 25 $cm^3$ were filled with about 95 g of solution. After homogenizing the solution, its saturation temperature was accurately determined in a similar way to that described above for single crystal growth. For this solution composition, the saturation temperature was around 1145 K. The (001) RTP substrates were first cleaned by using a mixture of $HNO_3$/$H_2O$ in the 50/50 ratio in volume for 5 min, followed by dipping in distilled water (5 min), then in acetone (5 min), and finally in ethanol (5 min). The entire cleaning process was carried out with the substrates rotating at 60 rpm. After that, the substrates were slowly introduced into the furnace using a stepper motor drive to avoid thermal shocks. This process can take 10-12 h depending on the selected speed of motor. Before dipping the substrate into the solution, it was maintained at a few mm above the surface of the solution for at least 1 h in order to obtain thermal equilibrium between the solution and the substrate. Then the substrate was dipped into the solution at a temperature of 1 K above the saturation temperature for 5 min in order to dissolve the outer layer of the substrate. The epitaxial growth was carried out on the RTP substrate at a temperature 3 K below the saturation temperature for 3 h, with the substrate rotating at 60 rpm. After the epitaxial growth process, the sample was withdrawn very slowly from the solution and held a few mm above the solution, whereas the furnace was cooled down to room temperature at a rate of 25 K/h, to avoid thermal shock.

RTP single crystals were obtained by the TSSG-SC technique with dimensions around 16 mm x 20 mm x 15 mm along the crystallographic ***a***, ***b*** and ***c*** directions, respectively. These crystals were transparent, without macroscopic defects and with well-defined morphology, as can be seen in Fig. 1a. After obtaining these crystals, several (001)-oriented substrates were cut and polished, resulting in an average roughness of 15 nm.

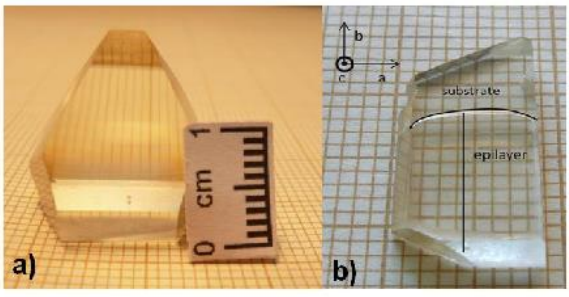


Fig. 1. (a) RTP single crystal, (b) As-grown (Yb,Nb):RTP/RTP epitaxial layer.

The growth rate of the epitaxial layers, after creating a supersaturation by keeping the growth temperature to 3 K below the saturation temperature, was around 0.3 μm/min. The epitaxial layers were polished down to 5 μm thickness after the growth, in order to achieve single mode guiding. A 9-mm-long epitaxial layer grown on a RTP(001) substrate,

polished to 5-10 µm thicknesses, is shown in Fig. 1b. In the polished epitaxial layers, the obtained surface roughness was around 5 nm.

*B. Pattern design and simulation*

The design of the patterns is shown in Fig. 2. A balanced single mode MZI design without any geometrical path length difference between the two arms and with two identical symmetric Y-structures, in which one acts as a splitter and one as a combiner, is shown in Fig. 2.a. Fig. 2.b shows a Y-structure with similar design parameters to act only as a splitter. We have designed MZIs and Y-splitters of length 9 mm with radius of curvature ranging from 50 to 80 mm. It was expected that the Y-junction design, based on an S-line pattern, would give low losses and a large enough separation between the two arms so that there is no evanescent coupling between the branches. It was also expected to give the maximum length in the branches for future applications as an electro-optical modulator. To ensure single-mode behavior of the MZI and Y-splitters at the selected wavelength, the core width and height of the waveguides must be limited depending on the refractive contrast Δn between the waveguide core and the substrate.

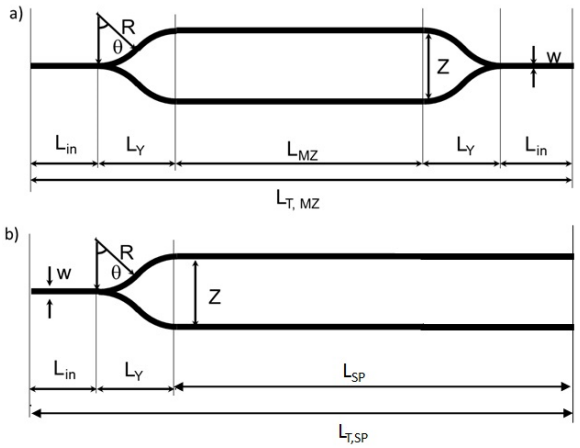


Fig. 2. (a) MZI and (b) Y-splitter design.

The guiding properties of the MZIs and Y-splitters were modelled with RsoftBeamPro [20] at a wavelength of 1.5 µm. The dimensions of the designed structures are channels with a width from 6 to 9 µm, and 5 µm in depth. These dimensions were chosen in order to support a fundamental guided optical mode at a wavelength of 1.5 µm. The parameters of the designs are given in Table I.

TABLE I
Parameters of the design.

| MZI | Dimensions [µm] | Y-splitter | Dimensions [µm] |
|---|---|---|---|
| $L_{in}$ | 1000 | $L_{in}$ | 1000 |
| $L_Y$ | 2000 | $L_Y$ | 2000 |
| $L_{MZ}$ | 3000 | $L_{SP}$ | 6000 |
| w | 6 | w | 6 |
| $L_{T,MZ}$ | 9000 | $L_{T,SP}$ | 9000 |
| Z | 38-42 | Z | 38-42 |
| R | 50,000-80,000 | R | 50,000-80,000 |

*C. Sample preparation prior to reactive ion etching procedure*

Prior to fabrication of waveguides by RIE, the RTP samples were clamped on a glass substrate using Unibond power epoxy resin. This step is necessary due to the relatively small size of the samples, which makes it difficult to handle them in spin coating and photolithography processes and reduces the edge bending effect. The curing time of epoxy was around 6-7 h and it allowed heating to 423 K without detachment from the glass. Finally, the sample was cleaned with acetone and iso-propanol using a sonicator.

In order to obtain deep etching, it is necessary to use a highly selective metal mask. We have evaluated Ti, Ni, Al and Cr metals as possible candidates for the metal masks. Metal layer deposition was performed by E-beam evaporation and sputtering techniques. Metal surfaces were evaluated by a molecular imaging atomic force microscope (AFM), model Pico SPM II, without any previous sample preparation, using acoustic mode at a resonance frequency of 75 KHz and a silicon tip of 10 nm radius. The topography and surface roughnesses of the deposited metal layers, analysed by AFM, are shown in Fig. 3. Surface roughness *rms* values calculated with the help of WSxM software were 2.8 nm, 2.6 nm, 150 nm and 100 nm for Ti, Ni, Al and Cr layers, respectively. As observed, for the case of Ti and Ni there are almost flat layers, but in the case of Al and Cr, the layers are composed of grains; which are larger for Al. The presence of these grains leads to the higher value of roughness for Al and Cr layers.

In order to analyze the adhesion and durability of the metal layers on the RTP surface, we performed a tape test five times each to check the adhesion. The Ti layer was completely or partially removed during the first attempt, as can be seen in Fig. 3. In the case of Ni, in the first attempt only significant parts of the Ni layer were removed but in second attempt, Ni was removed as can be observed in Fig. 3. A scratch test was also performed on the Ni layer but didn't show any significant influence on the adhesion. Finally, in the case of Al and Cr there was not observed removal of the metal during the tape tests. The scratch test on Al and Cr layers showed a good adhesion in both cases.

Thus the results indicate that Al and Cr are good candidates to be used for metal mask. In order to create a metal mask for the RIE process, the chromium was etched with MS8 chrome chemical etchant and the aluminum was etched with commercially available aluminum enchant.

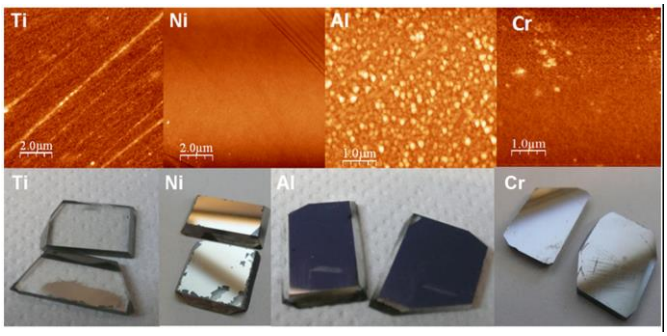


Fig. 3. AFM images of the different metal layers and the results of adhesion tests.

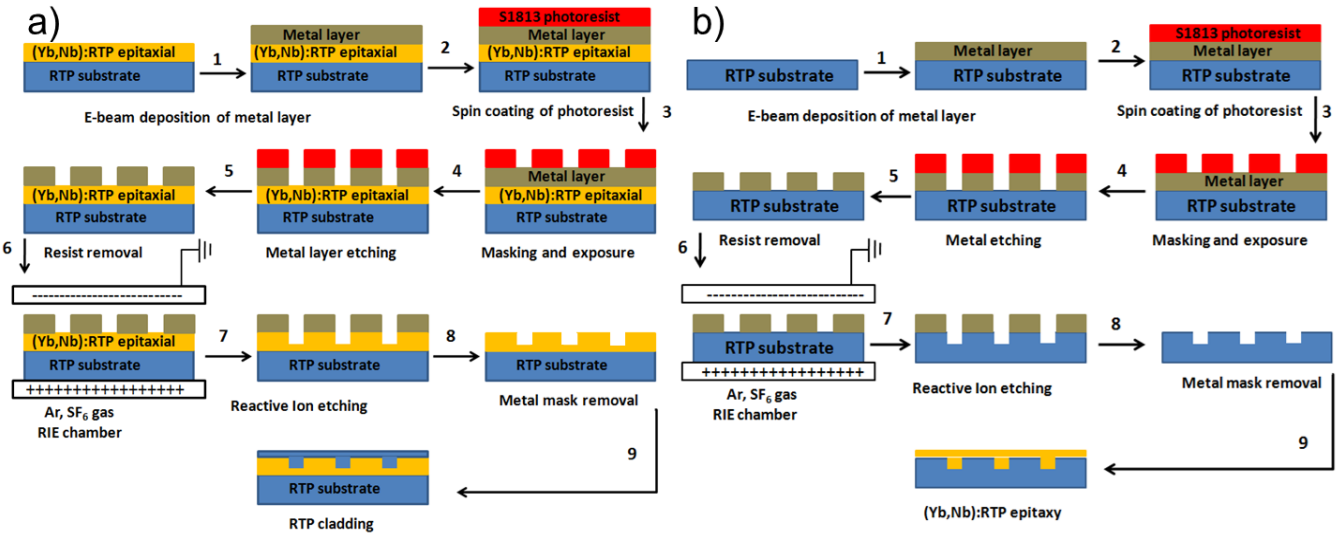


Fig. 4. Steps involved in the fabrication process of the rib waveguides (a) in a (Yb,Nb):RTP epitaxial layer ( b) in a RTP substrate.

A thin layer of photoresist S1813 was then deposited on the metal layer by spin coating at 5000 rpm for 60 s, obtaining photoresist thicknesses of around 1.3 µm. The samples were then soft baked at 363 K for 30 min.

Y-splitter and MZI patterns were transferred to the photoresist layer using a light field hard mask pattern for the epitaxial layers and a dark field hard mask pattern for the substrates, by standard UV photolithography. The samples with the photoresist and metal layers were carefully aligned with the mask pattern in such a way that the branches of the MZI and Y-splitters were parallel to the ***a*** crystallographic direction. A SussMicrotec MA6 mask-aligner was used to expose the samples for 10-12 s at 350 mW/cm$^2$, using 365-nm-wavelength light. After the exposure, the photoresist was developed by dipping for 45 s in MF-319 developer. Finally, hard baking was performed for 30 m at 393 K.All fabrication steps are illustrated in Fig. 4.

*D. Reactive ion etching*

The samples containing hard metal mask were etched in an RIE Plasmalab 80Plus, with the etching parameters: 250 W as the RF power, 40 mTorr of pressure and a gas combination of Ar (10 sccm) and $SF_6$ (10 sccm), which corresponds to parameters optimized in our previous work [15]. A preliminary test was performed to determine the etch rates in (Yb,Nb):RTP, undoped RTP, the metal layers and the photoresist using the etching conditions described above. The samples were etched for 60 min and the etch rates obtained are summarized in Table II.

The selectivity (the ratio of the etch rate of RTP compared to the etch rate of the photoresist) for RTP compounds against the photoresist is around 3. This means that it would require a thickness of photoresist around 20 µm to etch 6 µm in RTP, so it is not possible to obtain a smooth and homogeneous thick layer using specifically this photoresist eliminating the possibility of working with this photoresist as a mask. The selectivity for RTP against Cr was found to be 20 and the selectivity for (Yb,Nb):RTP against Cr was found to be 29. For Al, the selectivity against RTP was 5 and against (Yb,Nb):RTP was 7.8. It has previously been reported [21] that Al masks used in RIE processes using $SF_6/O_2$ gases show the effect of micromasking if the etched matter from the mask

TABLE II
RIE etch rates

| | Etch rate [nm/min] |
|---|---|
| **RTP** | 10.5 |
| **(Yb,Nb):RTP** | 15.5 |
| **PR S1813** | 36.6 |
| **Chromium** | 0.53 |
| **Aluminum** | 2 |

is not properly evacuated and is instead deposited the formed $Al_2O_3$ on exposed surfaces. Using $SF_6$, we can also create the AlF volatile species and the $AlF_3$ as non-volatile species, which can originate also the micromasking.

Table III summarizes all the RIE experiments performed with the different experimental parameters. Extended topography measurements of the channels were performed using a Sensofar PLµ 2300 confocal microscope. The confocal microscope was also used to measure the epitaxial thicknesses. The plasma etching involves two dominant etch mechanisms: physical and chemical. The physical mechanism is the high-energy ion bombardment that erodes the material and the chemical mechanism is the formation of volatile species from reactions on the material surface with the species from the plasma. We expect the volatile species to be $TiF_4$ (Temperature of sublimation 557 K), $PF_3$ (Boiling point 172 K), $NbF_5$ (Boiling point 502 K) and $PF_5$ (Boiling point 198 K) [22]. As mentioned above, the RIE process employed 250 W RF power, 40 mTorr pressure and gas combination of Ar (10 sccm) and $SF_6$ (10 sccm).

In Fig. 5, we can observe the etch rate obtained in undoped RTP and (Yb,Nb):RTP in relation to the etching time used. As can be seen in Table III, the average etch rate obtained is in the range of 3.2 to 8.7 nm/min; this etch rate is larger than previously reported for standard RIE of $LiNbO_3$ (around 4 nm/min) [23], although we note that the etching rate of $LiNbO_3$ can be increased after proton exchange to values of 10 nm/min [24]. It can be observed that in the case of short etching times, there is a linear reduction in the etching rate with the time. The potential causes of the low etch rate include too high a pressure of the etching gases, increasing the number

TABLE III
Parameters obtained for the etched designs

| Sample | Compound | M | $t_{epi}$[μm] | t [min] | $w_{exp}$ [μm] | $w_r$ [μm] | d [μm] | Etch rate [nm/min] |
|---|---|---|---|---|---|---|---|---|
| Sample 1 | (Yb,Nb):RTP | Cr | 3.2 | 213 | 4 | - | 1.8 | 8.2 |
| | | | | | 6 | - | | |
| Sample 2 | (Yb,Nb):RTP | Cr | 8.8 | 387 | 4 | 7.5-10 | 2.6 | 6.7 |
| | | | | | 6 | | | |
| Sample 3 | (Yb,Nb):RTP | Cr | 5 | 333 | 5 | - | 2.8 | 8.4 |
| | | | | | 7 | - | | |
| Sample 4 | (Yb,Nb):RTP | Cr | 5 | 333 | 4 | - | 2.9 | 8.7 |
| | | | | | 6 | - | | |
| Sample 5 | (Yb,Nb):RTP | Al | 5 | 624 | 7 | - | 2.5 | 4.0 |
| Sample 6 | RTP | Al | - | 480 | 5 | 13-15 | 2.5-3.5 | 6.2 |
| | | | | | 7 | | | |
| Sample 7 | RTP | Al | - | 810 | 5 | - | 2.6 | 3.2 |
| | | | | | 7 | | | |

M= metal, $t_{epi}$ = epitaxial layer thickness, t = etching time, $w_{exp}$ = expected width, $w_r$ = real width and d = etching depth

of collisions in the gas and a decreasing the number of reactive species reaching the surface and another possible reason, could be an increase of the chemical etching, leading to the formation of sub-products acting as inhibitors on the surface of the etch material, blocking the etching process. Furthermore, in the case of long etching times, there is a significant decrease of the etching rate, both for undoped RTP and (Yb,Nb):RTP. This could be related to the fact that at long etching times, the etching was not only in vertical direction but also in the plane of the sample.

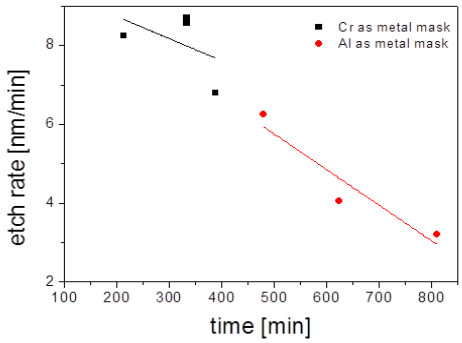


Fig. 5. Etching rate in undoped RTP and (Yb,Nb):RTP versus etching time.

According to Ren *et al*. [11], during RIE etching using gases such as $SF_6$, $CHF_3$, etc, gas components could penetrate into the sample, in our case to form bonds with the RTP sample. In order to detect any contamination of the sample by these gases, we have conducted an EDAX test using a FEI Quanta 600 equipment, with an acceleration voltage of 20 kV at a working distance of 10 mm. Sample 7 in Table III was examined for the detection of Al, Cr, Rb, Ti, O, P, S, F and Ar. Fig. 6 shows an ESEM image of this sample and the energy dispersive X-ray spectroscopy result where it can be observed that only the peaks of the constituent elements of the sample have been observed. There was no detected presence of any element originating from the gases (S, F, and Ar) or from the hard mask (Al).

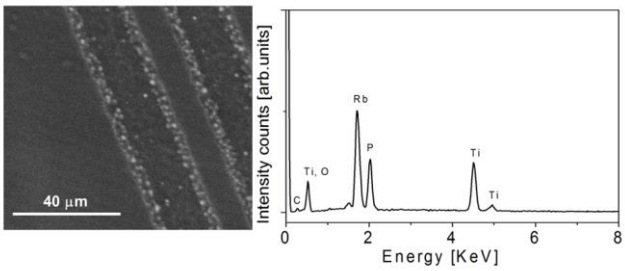


Fig. 6. Energy dispersive X-Ray spectroscopy of etched RTP sample using Al mask (sample 7).

The dimensions of the fabricated structures were evaluated by confocal interferometry, and the results are given in Table III. Width and depth were measured for every device (MZI and Y-splitter). The actual width was observed using an ESEM in sample 2 and sample 6. It is observed that the width of the structures is always larger than expected, especially in the case of the Al mask. In order to elucidate the reason for these results, different photoresist exposure times on the different metal layers were investigated. It was observed that longer exposure times lead to a larger broadening of the channels for the Al mask than in the case of Cr. It can be deduced that Al required less exposure time in order to obtain the desired width of the channels in the photoresist and this can be related to the larger reflectivity (R) of the Al versus Cr in the UV region (R of Al is 92% and R of Cr is 51%). The broadening of the channels obtained in the case of an Al mask could also be due to the fact that, as shown in Table II, the etching rate of Al is larger than for Cr. Therefore, in the case of long etching times, the Al layer could be totally removed, causing etching of the RTP material to take place along the plane as well as perpendicular to the surface.

The surface topography of the rib waveguide for sample 2, measured with confocal microscope, is shown in Fig. 7.a. The epitaxial layer roughness before etching was measured to be around 5 nm and after reactive ion etching it was around 15 nm. After the fabrication process, the samples were examined

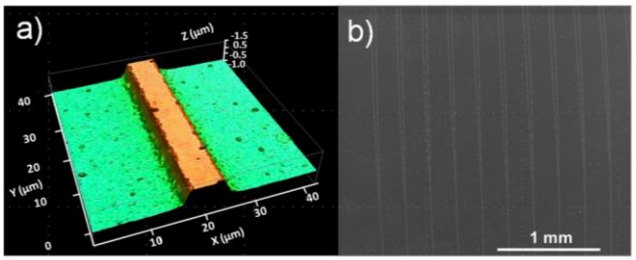


Fig. 7. (a) Surface topography of the rib waveguide obtained in (Yb,Nb):RTP (sample 2) measured with confocal microscope. (b) ESEM image of the top view of (Yb,Nb):RTP (sample 2) etched with RIE, with a power 250 W, and $SF_6$ 10 sccm, Ar 10 sccm and pressure 40 mTorr.

by environmental scanning electron microscopy (ESEM) with a FEI Quanta 600, with an acceleration voltage of 20 kV at a working distance of 10 mm. An ESEM image of the set of 9-mm-long MZIs fabricated on the (Yb,Nb):RTP deposited on RTP (sample 2) is shown in Fig. 7.b. It can be seen that rather homogenous etching is obtained along the full length of the MZI interferometers.

*E. Cladding layer growth*

A cladding layer of 200-400 μm thickness of RTP was grown on the channels in order to have centered the mode vertically on the active core region. The cladding would also serve as a protective material, and as demonstrated below by reducing the roughness of the core, it lowers the propagation losses. This cladding layer was grown by following the same procedure as used for the epitaxial layer.

In Fig. 8, an ESEM image of the cross section of an RIE channel realized in a (Yb,Nb):RTP/RTP epitaxial layer (sample 2) is shown. A cladding layer of undoped RTP was also grown on the (Yb,Nb):RTP etched layer. After etching for 387 min, an etch depth of around 2.6 μm in an 8.8-μm-thick epitaxial layer is obtained. As can be observed in Fig. 8, the slab height is around 6 μm with a rib height of 2.6 μm. The channel width is 7.3 μm at the base, making a trapezoid with an angle of 30º. As in the previous case, no visible defects are observed in the interface between the active layer and the cladding.

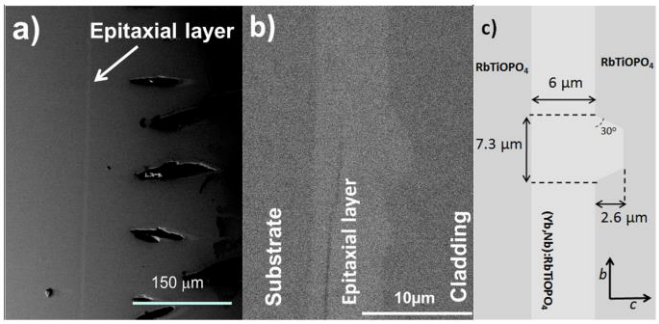


Fig. 8. (a) ESEM image of the general view of the cross section of RIE etched (Yb,Nb):RTP layers and RTP cladding grown also by LPE. (b) ESEM image of the detail of the cross section of RIE etched (Yb,Nb):RTP layers and RTP cladding grown also by LPE. (c) Cross sectional dimensions of the Fig. 8(b).

In Fig. 9, we can observe a cross-sectional ESEM image of a channel fabricated by RIE in a RTP substrate (sample 6), using an Al mask with structures of 7 μm width. The etching time was 480 min and the etch depth obtained was around 2.5-3.5 μm. The next step was the growth of an (Yb,Nb):RTP layer by LPE. In this case, the solution composition for the layer growth was the same as that used for the epitaxial layer growth and the growth time was 2 h. The supersaturation of the solution was obtained by decreasing the solution temperature to 4 K below the saturation temperature. After another polishing step, a cladding layer of undoped RTP was also grown. Fig. 9 shows that ribs with trapezoidal cross sections were obtained and that there are no appreciable defects at both interfaces, between the epitaxial layer and the RIE etched substrate and between the cladding and the epitaxial layer. The bottom of the channels is found to be approximately 13-15 μm in width, while the channels height is 2.5-3.5 μm and the side wall angle is around 20-30º.

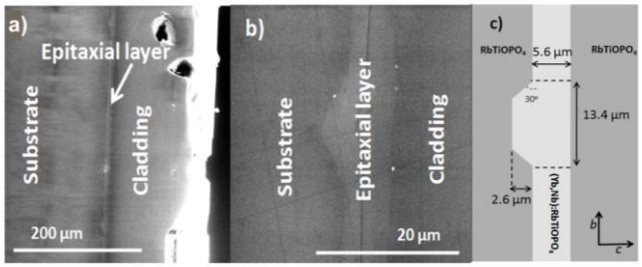


Fig. 9. (a) ESEM image of the general view of the cross section of RIE channels on RTP filled by (Yb,Nb):RTP by LPE and RTP cladding grown also by LPE. (b) ESEM image of the detail the cross section of a RIE channel on RTP filled by (Yb,Nb):RTP by LPE and RTP cladding grown also by LPE. (c) Cross sectional dimensions of the channel of Fig.9 b.

## III. OPTICAL CHARACTERIZATION OF THE WAVEGUIDES

Refractive index values at room temperature were measured in undoped RTP and in (Yb,Nb):RTP active layers with a Metricon prism coupler 2010 and a 1.5 μm HeNe laser by the dark mode method. The refractive index difference between the undoped RTP and (Yb,Nb):RTP doped crystals at a wavelength of 1.5 μm were calculated from the refractive index values of undoped RTP acting as a substrate: $n_x$=1.7559, $n_y$=1.7630, $n_z$=1.8375 and (Yb,Nb):RTP acting as an active epitaxial layer $n_x$=1.7516, $n_y$=1.7633, $n_z$=1.8425. Thus, $\Delta n_x$=-0.004, $\Delta n_y$=0.0003 and $\Delta n_z$=0.005 ($\Delta n_i = n_{i,epi} - n_{i,sub}$ being i= x,y and z). The increase of refractive index almost only in the $n_z$ polarization with the presence of Nb in RTP is in agreement with previous works in the literature [25, 26] and in KTP, as well [27], in which was already observed an increase of the birefringence in these crystals (defined as $n_z$-$n_x$ or $n_z$-$n_y$) with the increase of Nb concentration in the crystals (The Yb presence doesn't change this tendency). So, it is important to remark that this refractive index difference allows only guiding in the TM polarization whatever the size of the waveguide but it will be single mode by choosing the appropriate channel waveguide dimensions. Additionally, by using the standard definition for the NA of a fiber ($NA = (n_{core}^2 - n_{crystal}^2)^{1/2}$), the corresponding expected NA is of 0.13.

A vertically polarized (polarization parallel to the Z-axis of the samples) 1.5 µm He-Ne laser with a maximum output power of 1 mW, was coupled into the 9-mm-long devices. The input and output objectives were 5X with 0.10 NA and 20X with 0.40 NA, respectively. The 0.10 NA input objective ensured good NA matching with that expected for the waveguides (~0.13 NA, see below), and also gave a focus spot diameter of ~18 µm (at $1/e^2$ intensity) which matches well with the expected mode field diameters (MFD) of the waveguides. The waveguide mode was excited via careful alignment using an *xyz* translation stage. Near-field mode imaging of the devices was recorded using a FLIR SC7000 IR camera.

Assuming a planar waveguide, the dispersion for a wave propagating along the guide [28], could be calculated using

$$\frac{2\pi}{\lambda}\left(n^2 - n_{eff}^2\right) = m\pi + \phi_{n_a} + \phi_{n_s}$$

where $m$ is the mode number, $d$ the thickness of the active layer, $\lambda$ the wavelength of the light in vacuum, in this case 1.5 microns, and $n_a$ and $n_s$ are the air and the substrate refractive indices, respectively, while $n$ is the refractive index of the guiding layer, and $n_{eff}$ is the effective refractive index of the propagation mode in the active layer and

$$\phi_{n_j} = arctg\left[\left(\frac{n}{n_j}\right)^{2\rho}\left(\frac{n_{eff}^2 - n_j^2}{n^2 - n_{eff}^2}\right)\right]^2$$

where j = a, s, and ρ = 1 for TM polarization. Next Figure shows the calculated number of modes from these equations for TM polarizations. To confine only one mode for TM polarization we can have a maximum thickness of 8.1 microns (shown in figure 10).

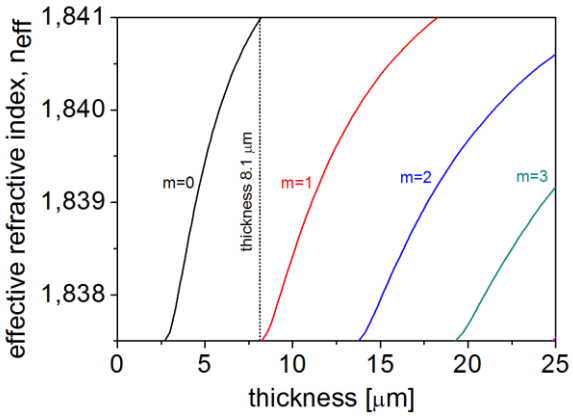


Fig. 10. Propagation modes versus the active layer thickness at 1.5 µm.

Then, going to the 2D waveguides, we use the simulations as a tool to optimize the other dimension, the width of the channel. Figure 11 shows the result of the simulation assuming a rectangular 2D channel, in which the *w* is 6 microns and the *h*, height is 5 microns (X, Y and Z are the optical axis of our samples, being the crystallographic **a**, ***b*** and ***c*** directions, respectively). The first graphic corresponds to the map of refractive index used; the second figure is the confined TM mode and last graphic shows the inexistence of the TE mode with the measured refractive contrast and with these dimensions. Then, the expected TM single–mode conditions, w=6 microns and height 5 microns, with an $n_{eff}$ around 1.839. These conditions of single mode are maintained till a width of 9 microns.

To experimentally characterize the propagation modes, we polished the faces perpendicular to the crystallographic ***a*** direction (X axis), and the light will propagate in this direction. The near field pattern was measured using an IR camera in order to visualize the mode intensity profile at the output of an MZI. Fig. 12.a shows the near-field pattern of the output TM mode guided in a MZI of the sample 2. The horizontal and vertical fundamental TM mode field diameters (MFD) at $1/e^2$ intensity (shown in Figs. 12.c and 12.d, respectively) were measured to be 17.6 µm and 8.3 µm, along the ***b*** (horizontal) and ***c*** (vertical) directions, respectively. Fig. 12.b shows the output TM mode obtained by the simulation. The dimensions of the simulated guided mode are 23.3 µm and 9.6 µm along ***b*** (horizontal) and ***c*** directions (vertical) respectively, and the refractive index contrast used is the one reported above for $n_z$, 0.005.

A 9-mm-long Y-splitter, fabricated in the sample 2, was also characterized as shown in Fig. 13.a. The Y-splitter is rather well balanced, obtaining an output flux power ratio between the two branches of 0.91. The horizontal and vertical fundamental MFD at $1/e^2$ intensity (shown in Figs. 13.c and 13.d, respectively) were measured to be 19 µm and 16.7 µm (right and left branches, respectively) along the ***b*** direction and 9.6 µm and 9.9 µm (right and left branches, respectively) along the ***c*** direction. The simulation of the modes is plotted in Fig. 13.b. The MFD for the simulated modes were 8.4 µm and 17.6 µm, for the vertical and horizontal directions, respectively. The separation between the centers of two modes emitting from two respective arms is around 36 µm.

We have estimated the total transmission losses

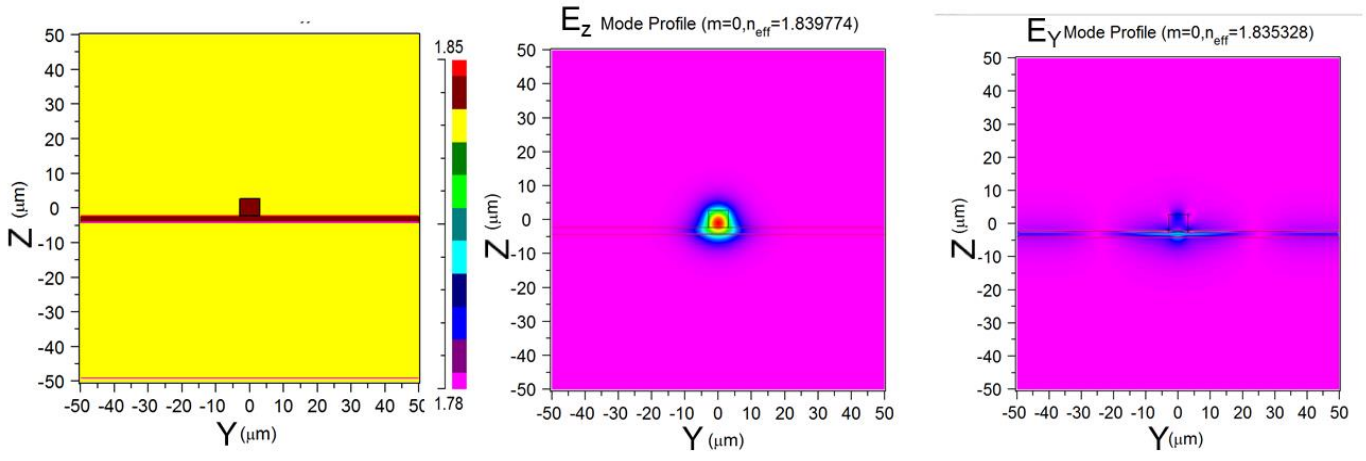


Fig. 11. Simulation of a rectangular 2D channel, with the *w* is 6 microns and the *h*, 5 microns (X, Y and Z are the optical axis of our samples, being the crystallographic **a**, ***b*** and ***c*** directions, respectively). (a) Map of refractive index, (b) Simulated TM mode, (c) Simulated TE mode.

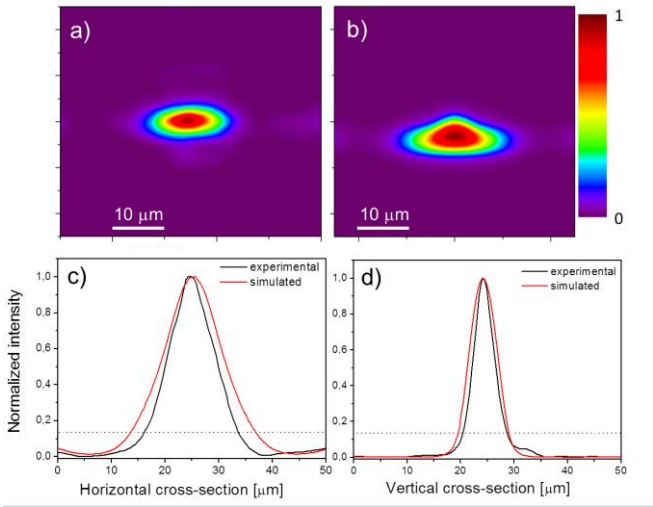


Fig. 12. (a) Near- field TM mode image of the waveguide MZI in the sample 2. (b) Simulated TM mode of the MZI waveguide in the sample 2, (c) Horizontal cross-section of the experimental and simulated TM guided mode, (d) Vertical cross-section of the experimental and simulation TM mode.

corresponding to a single pass transmission as $L_T$= 10log ($P_{out}/P_{in}$), where $P_{out}$ is the power measured after the output microscope objective, $P_{in}$ is the power measured before the input microscope objective. In the actual samples fabricated for this work, there are only MZ and Y-splitter structures as a WGs; so the total transmission losses measured should be the result of the addition of the optical insertion, the Fresnel and the propagation losses; and in the last term, are included the propagation losses of the straight portions of the MZ and the Y-splitter structures ($L_{in}$, $L_{MZ}$ and $L_{SP}$) and the propagation losses due to the S-bend and the Y-junction.

The optical insertion losses measured by calculating the $1/e^2$ overlapping between the input laser mode and the output guided mode; are around -1.2 dB for the MZ and -1.5 dB (left output) and -1.2 dB (right output), for the Y-splitter. The

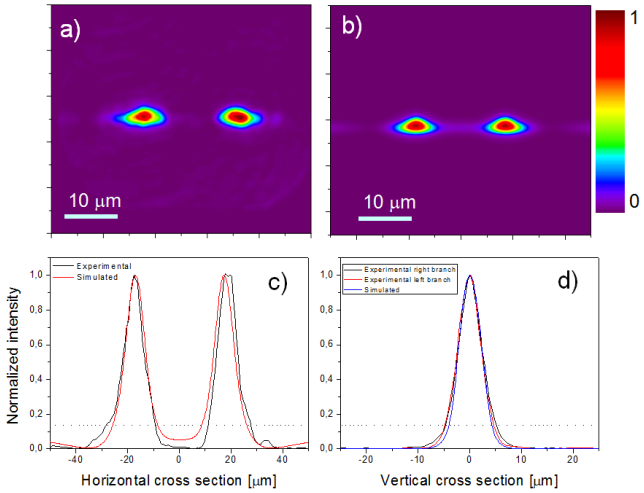


Fig. 13. (a) Near- field TM mode image of a waveguide Y-splitter in the sample 2, (b) Simulated TM mode of the Y-splitter waveguide in the sample 2, (c) Horizontal cross-section of the experimental and simulated guided TM modes, (d) Vertical cross-section of the experimental and simulation TM modes.

Fresnel losses are in both cases around -0.8 dB.

The measured total transmission losses, $L_T$, for the MZ were 8.75 dB. Accounting for the insertion losses (1.2 dB) and the Fresnel losses (0.8 dB) we can approximate the propagation losses as 6.7 dB, including the bending and Y-junction losses. For the Y-splitter, a measurement of the total transmission losses, gives us 7.08 dB, making a similar calculation, the total propagation losses (including bending and Y-junction) are around 4.9 dB (assuming 0.9 cm length, they are 5.4 dB/cm). These values are in agreement with the previous reported values, published by Choudhary *et al.* [15], in channel WGs fabricated also by RIE, in which the transmission losses were around >3.5 dB/cm at 980 nm.

## IV. CONCLUSIONS

Mach-Zehnder interferometer and Y-splitter structures have been successfully fabricated on RTP (001)-oriented substrates and (Yb,Nb):RTP/RTP (001) epitaxial layers using reactive ion etching. When RTP (001)-oriented substrates were used, an (Yb,Nb):RTP epitaxial layer was grown over the structures made by RIE and finally in both cases, a RTP cladding layer was grown by liquid phase epitaxy in order have the same contrast in the refractive indices in the two interfaces. The Cr and Al layer adhesion to RTP was suitable for transferring the structures from the commercial hard mask to the metal mask in contact with the crystal, before the RIE process was carried out. An etch depth of 2.9 μm with a maximum etching rate of 8.7 nm/min was obtained. The ribs were trapezoidal in shape with a roughness of about 15 nm. Optical waveguiding in the different fabricated structures at a wavelength of 1.5 μm has been demonstrated and characterized.

## REFERENCES


[1] P. A. Thomas, S. C. Mayo, and B. E. Watts, "Crystal structures of $RbTiOAsO_4$, $KTiO(P_{0.58},As_{0.42})O_4$, $RbTiOPO_4$ and $(Rb_{0.465},K_{0.535})TiOPO_4$, and analysis of pseudosymmetry in crystals of the $KTiOPO_4$ family," *Acta Cryst. B*, vol. 48, pp. 401-407, 1992.

[2] M. V. Pack, D. J. Armstrong, and A. V. Smith, "Measurement of the $X^{(2)}$ tensors of $KTiOPO_4$, $KTiOAsO_4$, $RbTiOPO_4$, and $RbTiOAsO_4$ crystals," *Appl. Opt.*, vol. 43, pp. 3319-3323, 2004.

[3] M. N. Satyanarayan, A. Deepthy, and H. L. Bhat, "Potassium titanyl phosphate and its isomorphs: growth, properties, and applications," *Crit. Rev. Solid State Mater. Sci*, vol. 24, pp. 103-191, 1999.

[4] W. P. Risk, "Fabrication and characterization of planar Ion-exchanged $KTiOPO_4$ waveguides for frequency doubling," *Appl. Phys. Lett.*, vol. 58, pp. 19-21, 1991.

[5] L. L. Wang, L. Wang, K. Wang, Q. Lu and H. Ma, "Annealing effect on mono-mode refractive index enhanced $RbTiOPO_4$ waveguides formed by ion implantation," *Opt. Express*, vol. 17, pp. 5069-5074, 2009.

[6] J. Jiao, K. M. Wang, X. L. Wang, F. Chen, L. Wang, L. Wang, Q. M. Lu, H. J. Ma, and R. Nie, "Optical waveguides formed in $RbTiOPO_4$ crystal by 6.0 MeV $O^{3+}$ implantation," *Chin. Phys. Lett.*, vol. 23, pp. 3327-3330, 2006.

[7] J. Cugat, R. Solé, M. C. Pujol, J. J. Carvajal, X. Mateos, F. Díaz, and M. Aguiló,"Waveguiding demonstration on Yb:Nb:$RbTiOPO_4$/$RbTiOPO_4$(001) epitaxies grown by LPE," *Opt. Mater.*, vol. 32, pp. 1648-1651, 2010.

[8] L. B. Zhou, F. G. Luo, and M. C. Cao, "Study of the plasma etching process for low-loss $SiO_2$/ Si optical waveguides," *Thin Solid Films*, vol. 489, pp. 229-234, 2005.

[9] C. Dubs, J. P. Ruske, J. Kräuβlich, and A. Tünnermann, "Rib waveguides based on Zn-Substituted $LiNbO_3$ films grown by liquid phase epitaxy," *Opt. Mater.*, vol. 31, pp. 1650-1657, 2009.

[10] G. Ulliac, N. Courjal, H. M. H. Chong, and R. M. De La Rue, "Batch process for the fabrication of $LiNbO_3$ photonic crystals using proton

exchange followed by $CHF_3$ reactive ion etching," *Opt. Mater.*, vol. 31, pp. 196-200, 2008.

[11] Z. Ren, P. J. Heard, J. M. Marshall, P. A. Thomas, and S. Yu, "Etching characteristics of $LiNbO_3$ in reactive ion etching and inductively coupled plasma," *J. Appl. Phys.*, vol.103, pp. 034109, 2008.

[12] C. Dubs, M. Morgenroth, B. Zeitner, J-P. Ruske, U. Grusemann, J. Delith, Chr. Schmidt, and. A. Tünermann, "Channel waveguides based on epitaxial grown $K_{1-x}Rb_xTiOPO_4$ LPE films," *Zeitschrift fúr kristallographie*, Issue No. 21, pp.189. 2004.

[13] M. Roth, "Stoichiometry and Domain Structure of KTP/Type Nonlinear Optical Crystals," in Handbook of Crystal Growth, Chapter 20, Springer Berlin Heidelberg, 2010, pp. 691-723.

[14] J. J. Carvajal, J. L. García-Muñoz, R. Solé, Jna. Gavaldà, J. Massons, X. Solans, F. Díaz, and M. Aguiló, "Charge Self-compensation in the Nonlinear Optical Crystals $Rb_{0.855}Ti_{0.955}Nb_{0.045}OPO_4$ and $RbTi_{0.927}Nb_{0.056}Er_{0.017}OPO_4$," *Chem. Mater.*, vol. 15, pp. 2338-2345, 2003.

[15] A. Choudhary, J. Cugat, K. Pradeesh, R. Solé, F. Díaz, M. Aguiló, H. M. H. Chong, and D. P. Shepherd, "Single-mode rib waveguides in (Yb,Nb):$RbTiOPO_4$ by reactive ion etching," *J. Phys. D*, vol. 46, pp. 145108, 2013.

[16] J. J. Carvajal, M. C. Pujol, and F. Díaz, "High Temperature Solution Growth: Application to laser and Nonlinear Optical Crystals" in *Handbook of Crystal Growth*, Chapter 21, Springer Berlin Heidelberg, 2010, pp. 725-752.

[17] J. J. Carvajal, V. Nikolov, R. Solé, Jna. Gavaldà, J. Massons, M. Aguiló, and F. Díaz, "Crystallization Region, Crystal Growth, and Characterization of Rubidium Titanyl Phosphate Codoped with Niobium and Lanthanide Ions," *Chem. Mater.*, vol.14, pp. 3136-3142, 2002.

[18] J. J. Carvajal, V. Nikolov, R. Solé, Jna. Gavaldà, J. Massons, M. Rico, C. Zaldo, M. Aguiló, and F. Díaz, "Enhancement of the Erbium Concentration in $RbTiOPO_4$ by Codoping with Niobium," *Chem. Mater.*, vol.13, pp.3171-3080, 2000.

[19] J. Cugat, R. Solé, J. J. Carvajal, M. C. Pujol, X. Mateos, F. Díaz, and M. Aguiló, "Crystal growth and characterization of $RbTi_{1-x-y}$/ $RbTiOPO_4$(001) non-linear optical epitaxial layers," *CrystEngComm.*, vol.13, pp. 2015-2022, 2011.

[20] RsoftBeamPROP software, Synopsys Optical solutions, v2013.12.

[21] M. Lazar, H. Vang, P. Brosselard, C. Raynaud, P. Cremillieu, J.-L. Leclercq, A. Descamps, S. Scharnholz, and D. Planson, "Deep SiC Etching with RIE," *Superlattices and Microst*, vol. 40, pp. 388-392, 2006.

[22] M. Köhler, "Etching in Microsystem technology", Weinheim; New York; Chichester; Brisbane; Singapore; Toronto, Wiley-VCH, 1999.

[23] S. Winnall, and S. Winderbaum, "Lithium Niobate Reactive Ion Etching", DSTO-TN-0291, DSTO Electronics and Surveillance Research Laboratory, Salisbury South Australia, 2000.

[24] H. Hu, A. P. Milenin, and R. B. Wehrspohn, H. Hermann, W. Sohler, "Plasma etching of proton-exchanged lithium niobate," *J. Vac. Sci. Technol. A*, vol. 24, pp. 1012-1015, 2006.

[25] J. J. Carvajal, R. Solé, Jna. Gavaldà, J. Massons, M. Rico, C. Zaldo, M. Aguiló and F. Díaz, "Growth and characterization of $RbTiOPO_4$:Nb crystals as a host for rare earth ions", *J. Alloy. Compd.*, vol. 323-324, pp. 231-235, 2001.

[26] A. Peña, "Ytterbium and erbium doped $RbTi_{1-x}M_xOPO_4$ (M = Nb or Ta) crystals. New laser and nonlinear bifunctional materials," Ph. D. dissertation, Dept. Phys. Chem. And Inorg., Rovira i Virgili Univ., Tarragona, Spain, 2007.

[27] L. T. Cheng, L. K. Cheng, R. L. Harlow and J. D. Bierlein, "Blue light generation using bulk single crystals of niobium-doped $KTiOPO_4$," *Appl. Phys. Lett.*, vol. 64, 155-157, 1994.

[28] P. K. Tien and R. Ulrich, "Theory of Prism-coupled and thin-film light guides," *J. Opt. Soc. Am.*, Vol. 60, pp. 1325-1337,1970.